Energy Advances

PAPER

View Article Online
View Journal | View Issue



Cite this: *Energy Adv.*, 2026, 5, 341

# Enhanced electrocatalytic performance of phosphorus and metal oxide-modified graphite electrodes for all-vanadium redox flow batteries

Yassine Seffar,[a] Elhoucine Elmaataouy,[a] Yuri Mikhlin,[b] Melina Zysler,[b] David Zitoun,[b] Jones Alami[a] and Mouad Dahbi*[a]

Received 27th December 2025,
Accepted 24th January 2026

DOI: 10.1039/d5ya00381d

rsc.li/energy-advances

This study evaluates the electrocatalytic performance of graphite powder (GP) electrodes modified with CoO, NiO, and oxygen-rich phosphorus functional groups (P-GP) to improve the sluggish $VO_2^+$/$VO^{2+}$ redox kinetics in vanadium redox flow batteries (VRFBs). Although these electrocatalysts have been extensively applied to graphite felt, their comparative activity on graphite powder, a lower-cost, structurally distinct material, has not been systematically examined. Their intrinsic catalytic behavior was assessed through cyclic voltammetry, electrochemical impedance spectroscopy, charge–discharge cycling, and polarization tests. Pristine GP delivered a coulombic efficiency (CE) of 89.11%, voltage efficiency (VE) of 88.01%, energy efficiency (EE) of 78.43%, and power density of 49 mW $cm^{-2}$. CoO- and NiO-modified GP improved performance with CE values of 92.5% and 90.79%, and power densities of 154 and 149 mW $cm^{-2}$, respectively. The P-GP electrode showed the best results, with CE of 94.41%, VE of 93.97%, EE of 88.72%, and power density of 167 mW $cm^{-2}$, while retaining ~96% CE over 90 cycles. This study highlights phosphorus-functionalized and metal oxide modification (CoO, NiO) in enhancing the electrocatalytic performance of graphite powder electrodes, while providing a clear comparative assessment of their intrinsic electrocatalytic activity on graphite powder electrodes.

## 1. Introduction

In response to mounting concerns regarding climate change and environmental degradation, there has been a significant proliferation of initiatives and policies across both societal and technological domains. These initiatives and policies are designed to expedite the transition from conventional fossil fuels to renewable and environmentally sustainable energy sources.[1–4] One of the essential strategies to address the challenge of integrating intermittent renewable resources into electrical grids involves advancing electrochemical energy storage technologies that are highly efficient, scalable, and capable of maintaining grid stability under variable generation conditions from sources such as solar and wind energy.[5,6]

Among various energy storage technologies available today, redox flow batteries (RFBs) have emerged as particularly promising for medium-to-large scale energy storage applications, owing to their notable advantages such as long cycle life, excellent scalability, decoupled power and energy characteristics, and enhanced safety profiles, making them especially suitable for integrating intermittent renewable energy sources into modern electrical grids.[7–9]

Vanadium redox flow batteries (VRFBs) represent the most developed and commercialized technology among the various redox flow battery systems, largely due to their unique ability to utilize the four stable oxidation states of vanadium ($V^{2+}$, $V^{3+}$, $VO^{2+}$, and $VO_2^+$) for energy storage. This distinctive use of vanadium in both the anolyte and catholyte effectively prevents cross-contamination between the electrolytes, which contributes significantly to maintaining long-term system performance and stability, thereby decoupling energy and power output, making them particularly advantageous for large-scale energy storage applications and integration with renewable energy sources. As a result, VRFB systems are increasingly the technology of choice for numerous large-scale energy storage demonstration projects worldwide, demonstrating their scalability, safety, flexibility, and ability to provide stable and reliable power over long periods.

During the charge–discharge process, the electrochemical reaction of $VO_2^+$/$VO^{2+}$ and $V^{3+}$/$V^{2+}$ redox couples occurs

[a] *Materials Science, Energy and Nano-engineering Department, Mohammed VI Polytechnic University, Ben Guerir, Morocco. E-mail: mouad.dahbi@um6p.ma*
[b] *Department of Chemistry, Institute for Nanotechnology and Advanced Materials (BINA), Bar Ilan University, Ramat Gan 5900002, Israel*

at the electrocatalyst surface, producing a cell voltage of 1.26 V.

$$VO^{2+} + H_2O \underset{\text{Discharge}}{\overset{\text{Charge}}{\rightleftharpoons}} VO_2^+ + 2H^+ + e^- \quad E_0 = 1.01\ \text{V } \textit{vs.}\ \text{SHE}$$

$$V^{3+} + e^- \underset{\text{Discharge}}{\overset{\text{Charge}}{\rightleftharpoons}} V^{2+} \quad E_0 = -0.26\ \text{V } \textit{vs.}\ \text{SHE}$$

$$VO_2^+ + H_2O + V^{3+} \rightleftharpoons VO_2^+ + 2H^+ + V^{2+} \quad E_0 = 1.26\ \text{V}$$

Nonetheless, despite its attractive features, the widespread deployment of VRFB systems is limited by challenges such as high system costs and the low intrinsic electrochemical activity of the electrocatalysts.[10–12]

The electrocatalyst is a key component in VRFBs and significantly impacts cell performance, as the redox reactions of vanadium ions occur at the electrocatalyst surface. Currently, polyacrylonitrile (PAN)-based graphite felt is the most widely used electrocatalyst material due to its high chemical stability in acidic electrolytes,[13] wide operating potential window, excellent electrical conductivity, and relatively large surface area. However, pristine graphite felt exhibits poor electrochemical kinetics, especially for the $VO_2^+/VO^{2+}$ redox couple, due to the complex reaction mechanism involving several elementary steps. Given these limitations, enhancing the electrochemical activity of graphite felt is critical to improving VRFB performance, and numerous strategies have been proposed. Among these, heteroatom doping of graphite felt (GF) has emerged as a widely explored approach, as it introduces active functional groups on the electrode surface and promotes redox kinetics.[14]

For instance, Xingrong *et al.*[15] developed phosphorus and nitrogen co-doped PAN-based graphite felt electrodes, which exhibited significantly enhanced energy efficiency, achieving a 7.9% improvement over pristine GF at a current density of 200 mA $cm^{-2}$.[15] Similarly, Kim *et al.* employed an impregnation–calcination method to introduce phosphorus-rich oxygen functionalities on GF, resulting in an energy efficiency of 88.2% compared to 83% for the unmodified electrode at 32 mA $cm^{-2}$.[16] An alternative approach involves integrating electrocatalytic materials onto the GF surface, encompassing both metal-free and metal-based catalysts.[17] Lian *et al.* reported the use of sulfonated carbon nanotubes ($SO_3$-CNTs) as metal-free electrocatalysts to promote $VO_2^+/VO^{2+}$ and $V^{3+}/V^{2+}$ redox reactions. The $SO_3$-CNT modified electrode yielded voltage and energy efficiencies of 81.46% and 78.83%, respectively, marking improvements of 6.15% and 6.12% over bare GF.[18] Other carbon-based catalysts, such as MOF-derived carbon,[19] three-dimensional carbon frameworks,[20] and activated carbon,[21] have also demonstrated promising results. In terms of metal-based electrocatalysts, various metal oxides such as $Mn_3O_4$,[22] $PbO_2$,[23] $WO_3$,[24] $TiO_2$,[25] $SnO_2$,[26] and $CoNiO_2$,[27] have been synthesized *via* chemical or physical techniques for VRFB applications. Notably, Seyedabolfazl *et al.* fabricated $WO_3$-coated GF electrodes using pulsed laser deposition to enhance the $VO_2^+/VO^{2+}$ redox couple kinetics. The modified electrode delivered a peak power density of 556 mW $cm^{-2}$ at a current density of 800 mA $cm^{-2}$.[24]

Graphitic carbon is an abundant, cost-effective material that has attracted considerable attention as an electrocatalyst for VRFBs. Graphite is a crystalline allotrope of carbon composed of layers of hexagonally arranged atoms bonded by strong covalent bonds, with layers held together by weak van der Waals forces.[28] Chemically inert, electrically conductive, and thermally stable, graphite is widely used in lithium-ion batteries,[29] Fuel cells,[30] and supercapacitors.[31] Graphite is highly conductive and catalytically active, but its hydrophobicity limits wettability and slows $VO_2^+/VO^{2+}$ redox kinetics. This poor interfacial contact impedes electron and ion transfer, reducing power as well as energy and voltage efficiencies in vanadium redox flow batteries. To overcome these limitations, nanoparticles or heteroatom functional groups are incorporated onto graphite surfaces. These modifications improve surface wettability and increase active-site density, thereby enhancing $VO_2^+/VO^{2+}$ reaction rates and overall battery efficiency. For instance, Park *et al.*[32] prepared edge-functionalized graphene nanoplatelets (E-GnP) from graphite flakes *via* a ball-milling process, demonstrating that selective oxygen functionalization at the edge sites significantly enhanced both $VO_2^+/VO^{2+}$ and $V^{3+}/V^{2+}$ redox reactions. The flow cell based on E-GnP exhibited an energy efficiency over 15% higher than that of untreated carbon felt at a current density of 50 mA $cm^{-2}$.[32] Similarly, Alazmi *et al.* reported the use of reduced graphene oxide (rGO), derived from graphite powder, as an efficient electrocatalyst for VRFBs, achieving voltage and energy efficiencies of 78.4% and 72.7%, respectively, at 100 mA $cm^{-2}$.[33] These studies underline the effectiveness of graphite-derived nanostructures in improving the electrochemical activity of VRFB electrodes and highlight the importance of edge-defect engineering and surface functionalization in achieving high-performance redox kinetics.

In this study, we investigated three types of surface modifications: phosphorus–oxygen-rich functional groups and Co/Ni oxides, which have previously been applied to graphite felt, and we extended this comparison to graphite powder electrodes to demonstrate a more cost-effective approach to evaluating electrocatalyst performance. Using an impregnation–calcination method, we assessed the catalytic activities of these modified electrodes specifically toward the $VO_2^+/VO^{2+}$ redox couple on the positive electrode. A combination of physical characterization and electrochemical techniques was employed to analyze surface morphology, functional group distribution, and redox kinetics. Full VRFB cells were assembled using both pristine and modified graphite electrodes to determine the impact of surface modification on battery performance, and the resulting electrochemical behavior and efficiencies were systematically investigated and discussed in detail.

## 2. Experimental

### 2.1. Material and synthesis

Cobalt(II) and nickel(II) nitrate hexahydrate (ACS reagent, ≥98%), vanadium oxide (97%), sulfuric acid (95–98%), diammonium hydrogen phosphate (99%), graphite powder (≥99.99%),

potassium chloride (99%), and graphite powder were obtained from Sigma Aldrich. For P-GP, 1 g of graphite powder was immersed in a solution of diammonium hydrogen phosphate and stirred for two hours. The mixture was dried for 5 h at 80 °C and heated at 500 °C for 2 h under argon gas flow. The resulting material was washed with distilled water and dried. For CoO/NiO-GP, 0.1 g of Co/Ni nitrate was added to 25 mL of water and ultrasonicated for 5 min, 2 g of graphite powder was added, and the solution was stirred for 2 h. The resulting mixture was dried at 80 °C for 6 h in a vacuum and subjected to two heating cycles – in air at 400 °C for 2 h, then under argon at 500 °C for 4 h.

### 2.2. Structural and morphological observations

A ZEISS 300 microscope was employed for scanning electron microscopy (SEM). The accelerating voltage was 15 kV, and the resulting images had a pixel size of 10 μm. The size and morphology were examined by a JEOL JEM 1400 transmission electron microscope (TEM) operated at 120 kV, and the distribution of nanoparticles (NPs) and local crystallographic phases from selected area electron diffraction (SAED) were examined by a JEOL JEM 2100 high-resolution TEM (HR-TEM) operated at 200 kV. For TEM and HR-TEM, a small quantity was dissolved in a few millilitres of ethanol and subjected to an ultrasonic bath for 15 min. A single drop of the obtained suspension was deposited on a carbon-coated copper grid with an eye dropper. The samples were placed in a vacuum chamber at ambient temperature prior to examination. X-ray photoelectron spectroscopy (XPS) was recorded with a NEXSA G2 surface analysis system with a monochromatic Al Kα X-ray source (1486.6 eV, 72 W, 400 μm spots). The Brunauer–Emmett–Teller (BET) method was used to analyze the specific surface area. $N_2$ sorption–desorption isotherms were used to measure the pore size distribution by the Barrett–Joyner–Halenda (BJH) method with the Micrometrics Gemini VII system. Raman spectra of bare and modified graphite samples were collected by laser excitation at 532 nm at room temperature in a range of 100–1500 $cm^{-1}$ with a Horiba LabRam instrument. Powder X-ray diffraction (XRD) was used to identify the crystal structure. XRD patterns were captured by a Bruker D8 ADVANCE diffractometer (30 kV, 10 mA) using Cu Kα radiation ($\lambda$ = 1.5406 Å). The data was registered in $2\theta$ of 20° to 80° with a step size of 0.01° with a 10 s count time.

### 2.3. Electrochemical measurements

The electrode slurry was prepared by mixing 80 wt% active material, 10 wt% carbon black Vulcan (XC72R, Cabot), and 10 wt% PVDF binder (Kynar 2801, Arkema). The components were combined with an appropriate amount of solvent and homogenized until a uniform mixture was obtained. The slurry was then cast onto SGL 29-AA carbon paper (SGL Carbon, Germany) using a doctor-blade coater. After coating, the electrode was dried at 80 °C under vacuum for 12 h. The typical mass loading of active material was maintained at approximately 2.0 mg $cm^{-2}$.

To investigate electrochemical behavior, cyclic voltammetry (CV) was conducted using a three-electrode cell consisting of the synthesis material as the working electrode, platinum wire as the counter electrode, and Ag/AgCl 3 M KCl reference electrode. The experiment involved sweeping the applied voltage at various scan rates from 10 to 80 mV $s^{-1}$. To perform electrochemical impedance spectroscopy (EIS) on the graphite electrodes, a three-electrode cell was employed using the procedure mentioned above over a frequency range of 100 kHz to 0.01 Hz with 10 mV amplitude. Electrochemical measurements were carried out using a Bio-Logic potentiostat (VMP-3e) with 0.7 M $VOSO_4$ catholyte in 2 M $H_2SO_4$.

The electrocatalytic effects of P, CoO, and NiO doping toward the $VO_2^+/VO^{2+}$ redox couple were assessed by analyzing the diffusion coefficients, the anodic and cathodic peak currents ($I_a$ and $I_c$), and the peak-to-peak separation ($\Delta E = E_a - E_c$), as summarized in Table 2. The diffusion coefficient was calculated using the Randles–Ševčík equation (eqn (1))

$$i_p = (2.687 \times 10^5) n^{3/2} A C (D\nu)^{1/2} \quad (1)$$

where $i_p$ is the current (A), $n$ is the number of transferred electrons, $A$ is the electrode surface area ($cm^2$), $C$ is the molar concentration of vanadium ions (mol $cm^{-3}$), $D$ is the diffusion coefficient ($cm^2$ $s^{-1}$), and $\nu$ is the scan rate (V $s^{-1}$). The capacitive and diffusion control was calculated by the Dunn equation (eqn (2))

$$i(\nu) = K_1\nu + K_2\nu^{1/2} \quad (2)$$

Battery performance tests were conducted using an electrolyte composed of 1.6 M of Vanadium oxysulfate and 4.3 M $H_2SO_4$, within a voltage window of 1.65–0.8 V, controlled *via* EC-Lab software (Bio-Logic). Electrocatalyst-modified graphite served as the positive electrode *vs.* an unmodified electrode (both with an effective area of 20 $cm^2$). A Nafion 117 membrane separated the two compartments. Each side of the cell contained 50 mL of electrolyte, which was independently circulated using pumps at a constant flow rate of 80 mL $min^{-1}$. Charge–discharge performance of all electrodes, including P-GP, CoO-GP, NiO-GP, and bare GP, was evaluated at current densities ranging from 25 to 200 mA $cm^{-2}$. Discharge polarization curves and peak power values were obtained as follows: the fully charged redox flow battery was discharged by sweeping the current density from 0 to 1000 mA $cm^{-2}$ at a rate of 1 mA $s^{-1}$, while recording the corresponding output voltage. After the sweep, the cell was allowed to rest for 2 minutes to reach a steady state at open-circuit voltage (OCV). Power density curves were generated by calculating the product of the output voltage and the corresponding current density at each point.

The Coulombic efficiency (CE), energy efficiency (EE), and voltage efficiency (VE) were calculated using the following equations:

$$\mathrm{CE}\ (\%) = \frac{C_d}{C_c} \times 100 = \frac{\int I_d \mathrm{d}t}{\int I_c \mathrm{d}t} \times 100 \quad (3)$$

$$\mathrm{EE}\ (\%) = \frac{E_d}{E_c} \times 100 = \frac{\int I_d V_d \mathrm{d}t}{\int I_c V_c \mathrm{d}t} \times 100 \quad (4)$$

$$\mathrm{VE}\ (\%) = \frac{\mathrm{EE}}{\mathrm{CE}} \times 100 \quad (5)$$

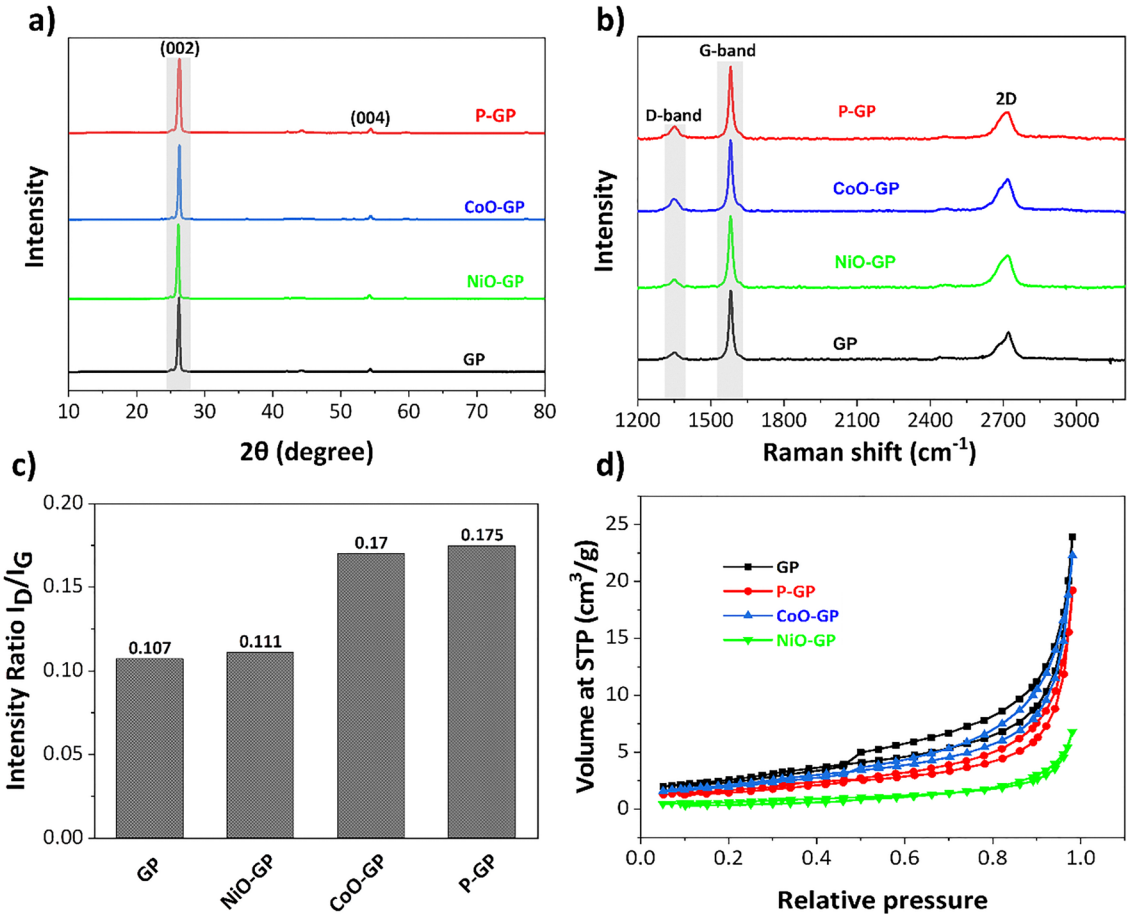


Fig. 1 (a) diffractogram, (b) Raman spectra, (c) corresponding intensity ratios ($I_D/I_G$), and (d) nitrogen sorption–desorption isotherms of the Bare graphite, P-GP, CoO/NiO-GP samples.

where $C_d$ and $C_c$ represent the discharge and charge capacities, respectively, while $I_d$ and $I_c$ are the discharge and charge currents, $E_d$ and $E_c$ refer to the discharge and charge energies, and $V_d$ and $V_c$ denote the discharge and charge voltages.

## 3. Results and discussion

### 3.1. Physical characterization

The diffractogram shown in Fig. 1a indicates that the bare graphite sample (GP) exhibits a broad peak around 25.5° corresponding to the (002) plane of graphite. This observation suggests that the carbon atoms in all samples are arranged in layers parallel to this plane. Furthermore, the presence of this peak at the same scattering angle in GP, P-GP, CoO-GP, and NiO-GP shows that the doping process had no significant effect on the graphite structure.

Raman spectroscopy was employed to examine the structural changes in the modified samples. Fig. 1b shows two distinct peaks at 1349 and 1580 $cm^{-1}$ corresponding to disorder (D) and graphitization (G) bands, respectively, with no significant Raman shift with dopant. The $I_D/I_G$ ratio is commonly used to evaluate the degree of structural disorder and provides an indication of the graphitic domain size. As presented in Fig. 1c, both the phosphorus- and cobalt-modified samples exhibit markedly higher $I_D/I_G$ ratios than pristine GP (0.17 *vs.* 0.11), while the Ni-GP sample shows a slightly elevated value. This increase can be attributed to the formation of defect sites on the graphite surface resulting from treatment with $(NH_4)_2HPO_4$ or from the incorporation of metal oxide nanoparticles.[16,34] To further investigate the textural properties of the electrode materials, pore size distributions were determined (Fig. S1), and the specific surface areas are summarized in Table S1. Fig. 1d displays the $N_2$ adsorption–desorption isotherms for all samples, which exhibit characteristic type-IV behavior. A substantial reduction in pore volume was observed after surface modification: the P-GP and NiO-GP samples show nearly a one-order-of-magnitude decrease compared to bare graphite, whereas the CoO-GP sample exhibits an approximately two-order-of-magnitude reduction. This decrease results from the deposition of oxygen-rich phosphorus groups and metal oxide nanoparticles, which partially block or fill surface defects and shallow mesopores on the graphite powder.[21] The lower BET pore volume does not reduce electrochemical activity because VRFB performance depends on surface catalytic sites, not on gas-accessible porosity. Added functional groups and metal oxides create new active sites, and

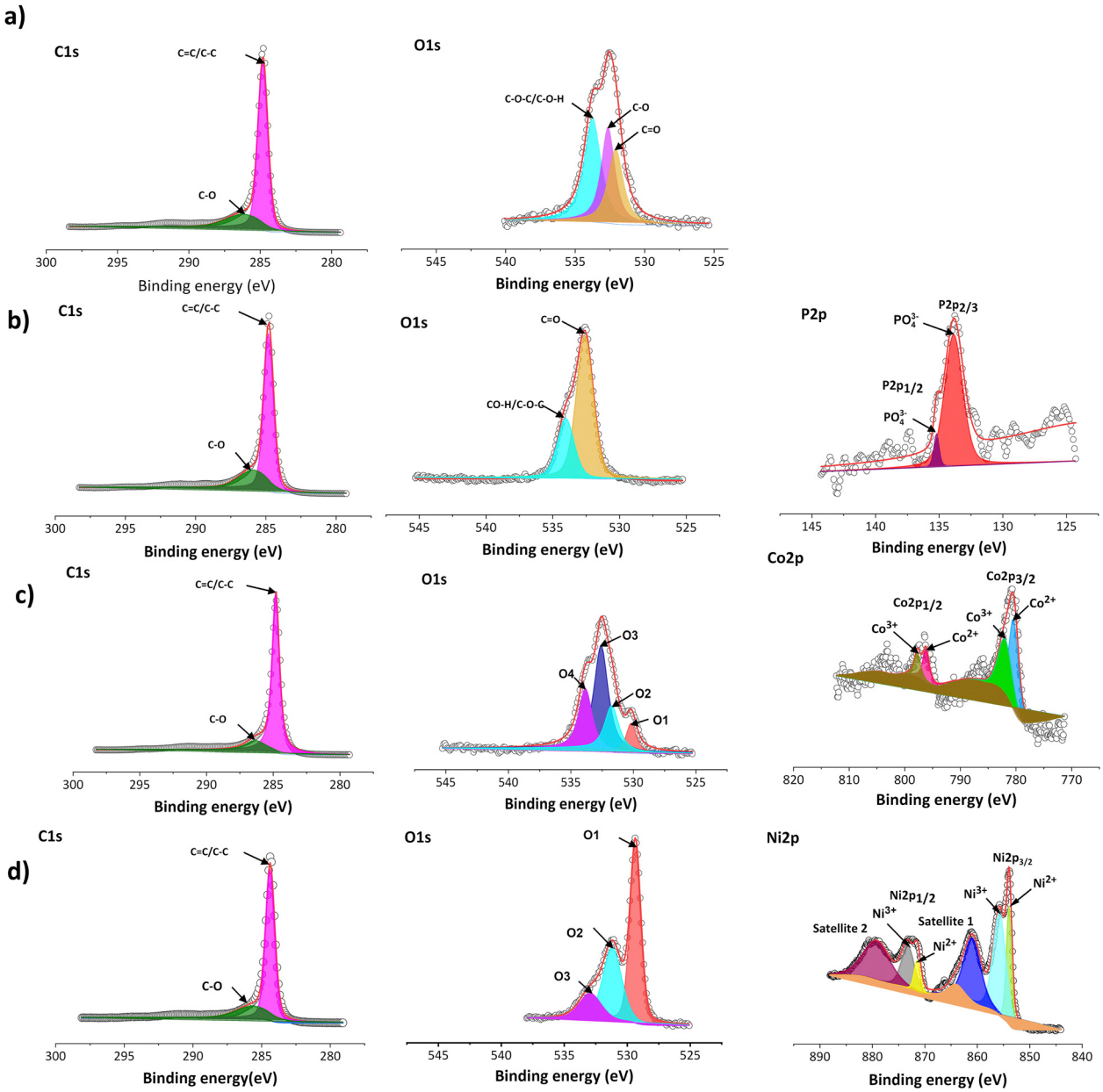


Fig. 2 High-resolution XPS spectra of (a) GP, (b) P-GP, (c) CoO-GP, and (d) NiO-GP.

ion transport is driven by electrolyte flow, so blocked pores do not hinder performance.

To better understand the atomic environment of the carbon surface, XPS measurements were carried out. Fig. 2 presents the O 1s and C 1s spectra of all samples, along with the P 2p spectrum for P-GP and the Co 2p/Ni 2p spectra for the CoO- and NiO-GP samples. The O 1s peak primarily originates from oxygen-containing species adsorbed on the graphite surface. As expected, a distinct phosphorus signal is observed on P-GP, while characteristic Ni and Co peaks appear on the NiO-GP and CoO-GP samples, respectively.

Fig. 2a shows the deconvolution of the C 1s and O 1s spectra, revealing peaks at binding energies of 284.8, 286.1, 532.1, 532.7, and 533.7 eV, which are assigned to graphitic C═C, C–O, C═O, C–O, and C–O–C/C–O–P functional groups, respectively. Fig. 2b illustrates that the P 2p region can be deconvoluted into two peaks corresponding to P $2p_{1/2}$ and P $2p_{3/2}$ at 133.8 and 135.2 eV, respectively, consistent with P–O bonding.[35,36]

The band at 533.7 eV may be attributed to C–O–P species in P-GP, indicating that phosphorus and carbon are likely connected through an oxygen bridge.[16] The O 1s spectrum of CoO-GP can be deconvoluted into four components: O1 (530.1 eV), O2 (531.7 eV), O3 (532.5 eV), and O4 (533.8 eV). O1 corresponds to lattice oxygen bonded to cobalt (Co–O), O2 is associated with surface hydroxyl groups, O3 is linked to oxygen species at defect sites with low coordination,[37] and O4 is assigned to carbon–oxygen bonding. In the Co 2p region, Co $2p_{3/2}$ and Co $2p_{1/2}$ peaks appear at 780.6 and 796.5 eV, respectively. The Co $2p_{3/2}$ peak can be deconvoluted into

two components at 780.4 and 782.0 eV, corresponding to $Co^{2+}$ and $Co^{3+}$, while the Co $2p_{1/2}$ peak can be similarly resolved into components at 796.1 and 797.7 eV. These features confirm the coexistence of $Co^{2+}$ and $Co^{3+}$, with the primary contributions arising from Co–O bonding.[37] For NiO-GP, the Ni $2p_{3/2}$ and Ni $2p_{1/2}$ peaks are observed at 853.8/855.7 eV and 871.3/873.2 eV, respectively, consistent with $Ni^{2+}/Ni^{3+}$ species.[38] Shake-up satellite peaks appear at 861.0 and 879.4 eV, further indicating the presence of NiO. The O 1s spectrum of NiO-GP can be deconvoluted into three peaks: O1 (529.3 eV), attributed to lattice oxygen bound to nickel; O2 (531.2 eV), possibly related to metal carbonate species; and O3 (532.9 eV), associated with C–O or C–O–H/Ni bonding. The presence of a C–O–Ni linkage, with characteristics similar to C–OH, suggests that some NiO nanoparticles are covalently attached to the graphite surface through hydroxyl ligands.[38]

Fig. 3 shows representative TEM images of all samples and the corresponding SAED patterns for the CoO-GP and NiO-GP materials. In Fig. 3a and b, the bare graphite (GP) sample displays parallel fringes associated with stacked graphite layers, each composed of graphene sheets. After the incorporation of oxygen-rich phosphorus groups, only minor changes in the layer arrangement are observed, consistent with the Raman results. The TEM images of CoO-GP and NiO-GP provide insight into the size, morphology, and dispersion of the metal oxide nanoparticles. As shown in Fig. 3e and f, the CoO nanoparticles exhibit a spherical morphology, good dispersion, smooth surfaces, and uniform particle sizes with an average diameter of 10–20 nm. Similarly, Fig. 3g and h shows that the NiO nanoparticles are also spherical, well-dispersed, and uniformly distributed across the graphite layers, with particle diameters in the range of 10–15 nm. Fig. 3k presents the SAED pattern of the CoO-GP sample, extracted from the HR-TEM image in Fig. 3i. The SAED rings display distinct speckled features characteristic of CoO nanoparticles. The first five rings (excluding the central spot) correspond to the (111), (200), (220), (311), and (222) lattice planes of CoO, confirming their polycrystalline nature. The broadening of the diffraction rings arises from the small particle size and the random orientation of the nanoparticles.[39] The SAED pattern of the NiO-GP sample is shown in Fig. 3l, taken from the HR-TEM image in Fig. 3j. The clearly defined diffraction spots indicate the presence of well-crystallized NiO nanoparticles. The indexed planes correspond to the (111), (200), (220), (311), and (222) reflections of NiO.[40] These results confirm the formation of crystalline NiO particles uniformly distributed across the graphite surface.

The wettability of an electrode is a critical factor determining the accessibility of aqueous electrolytes to its surface. Therefore, the wettability of GP and the modified electrodes was evaluated by measuring the static water contact angle, as shown in Fig. S5. The bare graphite (GP) exhibits a high contact

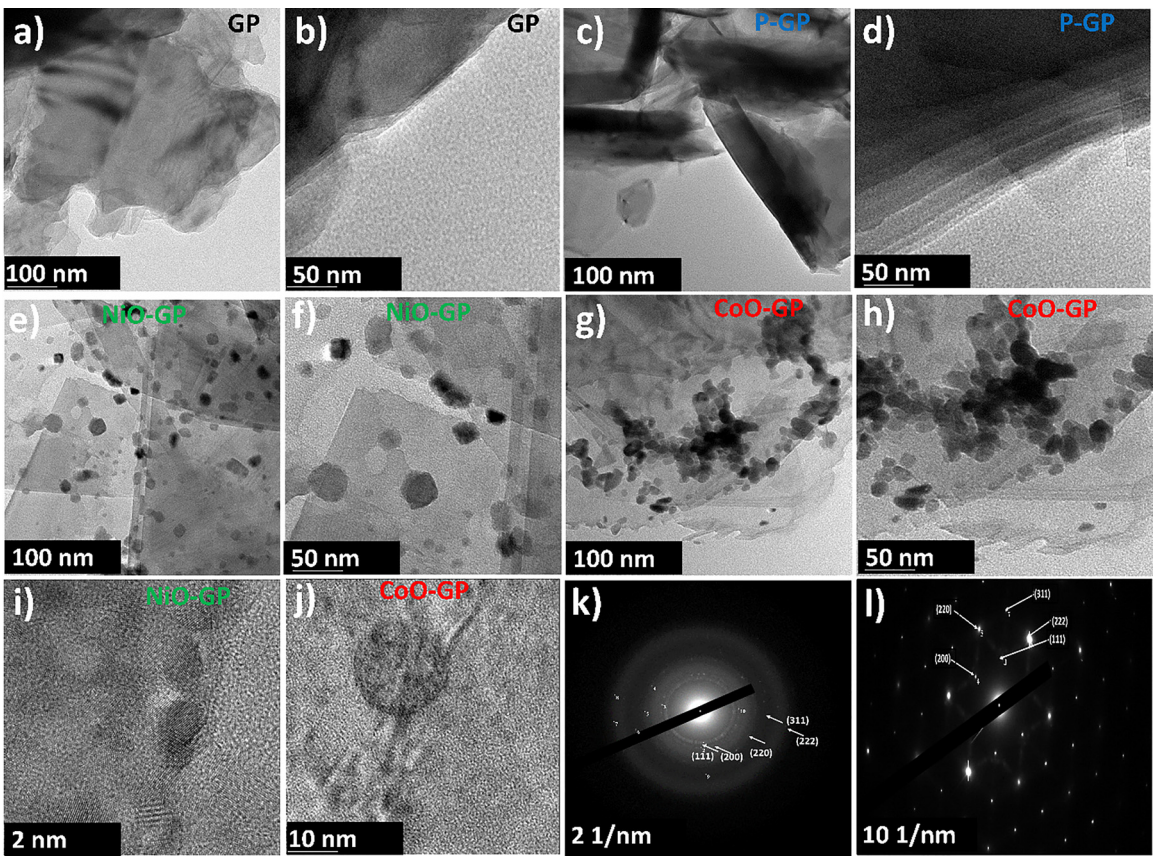


Fig. 3 TEM images of (a) and (b) bare graphite (GP), (c) and (d) P-GP, (e) and (f) NiO-GP, and (g) and (h) CoO-GP, and (i) and (j) HR-TEM images of CoO/NiO, respectively, and (k) and (l) SAED of CoO/NiO-GP.

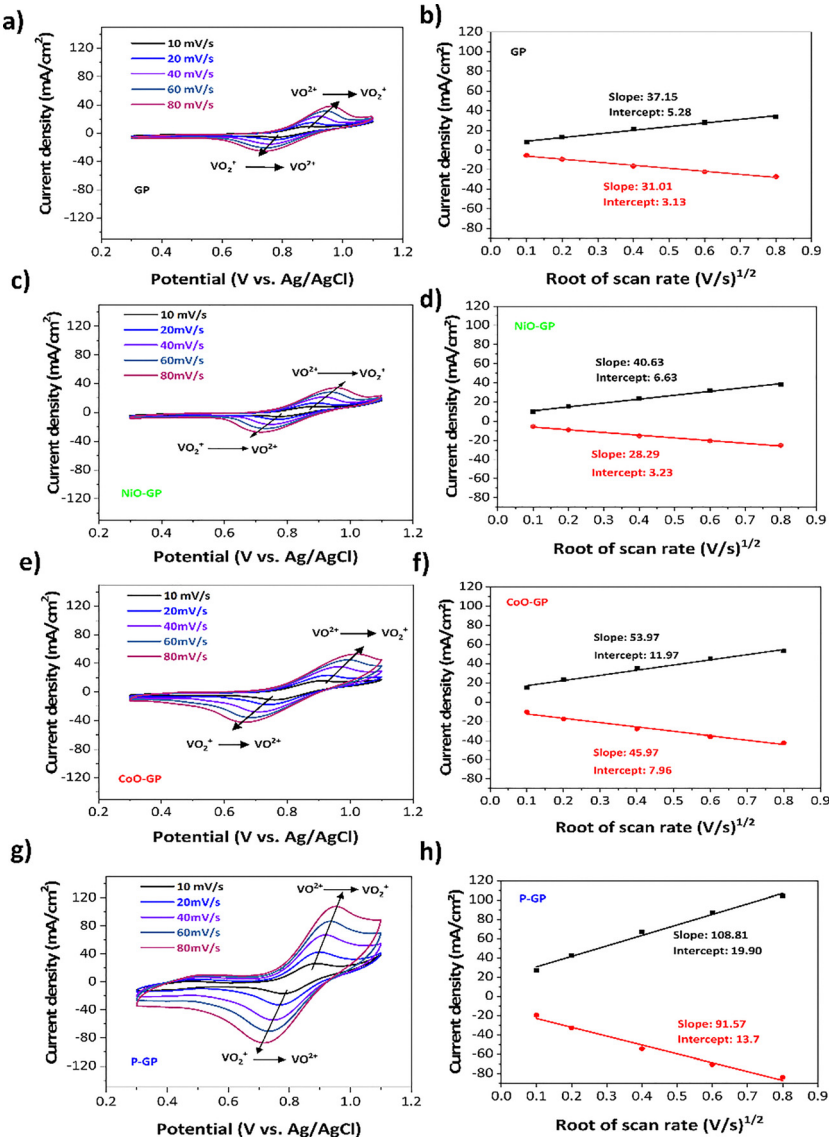


Fig. 4 Electrochemical measurements and electrocatalytic activity. Cyclic Voltammogram curves with potential window from 0.3 to 1.1 V *vs.* Ag/AgCl at scan rate from 10 to 80 mV $s^{-1}$ and peak current densities *versus* root scan rate of (a) and (b) bare graphite, (c) and (d) NiO-GP, (e) and (f) CoO-GP and (g) and (h) P-GP.

angle of 130.33°, indicating its hydrophobic nature. After the incorporation of phosphorus–oxygen functional groups, the contact angle decreases significantly to 67.66°, reflecting the increased hydrophilicity introduced by P═O and P–O groups, as well as the partial thermal reduction of the carbon surface. For the CoO-GP and NiO-GP samples, the contact angles also decrease, reaching 110.27° and 127.91°, respectively. This improvement can be attributed to the hydrophilic nature of CoO and NiO species and the effects of thermal treatment, which together enhance the overall surface wettability of the modified graphite.

### 3.2. Electrochemical performance

The oxidation and reduction peaks of the cyclic voltammogram for each sample are shown in Fig. 4a, c, e and g. The bare GP and NiO-GP electrodes exhibit low anodic and cathodic peak currents, indicating poor electrochemical kinetics for the $VO_2^+$/$VO^{2+}$ couple. In contrast, the P-GP and CoO-GP electrodes display more pronounced peak shapes and substantially higher peak currents. This enhancement is attributed to the improved electrical conductivity resulting from thermal treatment and the presence of oxygen-rich phosphorus groups and cobalt-oxide species, which introduce additional catalytic sites and facilitate faster electron transfer.

As shown in Table 1, the anodic peak current increases from 38.3 mA $cm^{-2}$ for bare graphite to 104.0 mA $cm^{-2}$ and 53.0 mA $cm^{-2}$ for the P-GP and CoO-GP electrodes, respectively, while NiO-GP shows only a slight increase to 39.5 mA $cm^{-2}$. Similarly, the cathodic peak current increases from −25.3 mA $cm^{-2}$ for GP to −83.9 mA $cm^{-2}$ and −42.4 mA $cm^{-2}$ for P-GP and CoO-GP. Moreover, the oxidation/reduction peak current ratio approaches unity for P-GP (1.24) and CoO-GP (1.25), compared with 1.51 for GP, indicating improved reversibility of the $VO_2^+$/$VO^{2+}$ redox couple.

Table 1 Relevant electrochemical parameters obtained from CV curves

| Electrocatalyst | $I_{pa}$ (mA cm$^{-2}$) | $I_{pc}$ (mA cm$^{-2}$) | Diff. coeff. ($10^{-8}$ cm$^2$ s$^{-1}$) | $I_{pa}/I_{pc}$ | $E_a$ (V) | $E_c$ (V) | $\Delta E$ (V) |
|---|---|---|---|---|---|---|---|
| GP | 38.3 | −25.3 | 5.3 | 1.51 | 0.97 | 0.73 | 0.23 |
| NiO-GP | 39.5 | −31.7 | 6.4 | 1.25 | 0.97 | 0.7 | 0.27 |
| CoO-GP | 53 | −42.4 | 11.2 | 1.25 | 1.03 | 0.66 | 0.36 |
| P-GP | 104 | −83.9 | 45.5 | 1.24 | 0.95 | 0.72 | 0.22 |

According to the Randles–Ševčík equation, mass-transfer characteristics can be evaluated by plotting the peak current against the square root of the scan rate, as illustrated in Fig. 4b, d, f and h. P-GP exhibits the largest slope, demonstrating that the oxygen-rich phosphorus groups enhance mass transport. This enhancement is attributed to the high electronegativity of oxygen relative to phosphorus, making P–O sites more favorable for cation adsorption.[41] Oxygen-containing groups also improve electrode wettability, thereby facilitating ion diffusion.[42] For CoO-GP, the slope is greater than that of GP, confirming the strong electrocatalytic activity of cobalt oxide. Vanadium ions are likely attracted to CoO surfaces through electrostatic interactions between positively charged vanadium species and negatively charged $O^{2-}$ species at CoO sites.[14] Overall, oxygen functional groups significantly enhance electron-transfer kinetics by promoting the adsorption of vanadium ions onto the electrode surface.[12]

Fig. S6 presents the contribution of capacitive and diffusion-controlled processes at different scan rates for GP and all modified materials, extracted from eqn (2), which distinguishes the terms $K_1\nu$ and $K_2\nu^{1/2}$ as the current contributions from capacitive and diffusion-controlled processes, respectively. Accurate determination of the constants $K_1$ and $K_2$ enables a quantitative evaluation of their influence on the current at a fixed potential. These constants were obtained from the slope and intercept of the linear regression of $i(v)/v^{1/2}$ *versus* $1/v^{1/2}$. Fig. S6b–h shows the specific contributions of capacitive and diffusion-controlled currents at a scan rate of 80 mV s$^{-1}$. The untreated GP sample exhibits a capacitive contribution of 48%, consistent with the presence of oxygen-containing functional groups (C–O and C═O), which provide active sites for the $VO_2^+$/$VO^{2+}$ redox couple. After incorporating CoO and NiO nanoparticles, the capacitive contribution increases to 66% and 85%, respectively. This enhancement is attributed to structural disruption caused by the nanoparticles, which partially occupy or block the graphite surface pores, as observed in Fig. S1. For the P-GP sample, the capacitive contribution decreases to 40%, while the diffusion-controlled fraction increases to 60%, exceeding that of bare graphite. This behavior explains the superior catalytic activity of P-GP. The phosphorus-containing P–O and P═O groups distributed on the graphite surface act as active sites for the $VO_2^+/VO^{2+}$ redox reaction, facilitating electron transfer and improving reaction kinetics.

The electrochemical kinetics of the $VO_2^+/VO^{2+}$ redox couple were further examined using electrochemical impedance spectroscopy (EIS). The Nyquist plots for P-GP, CoO-GP, NiO-GP, and GP are shown in Fig. S7, exhibiting a semicircle at high frequencies and a sloped line at low frequencies, indicating contributions from both charge-transfer and diffusion processes. The corresponding equivalent circuit includes $R_s$, representing the ohmic resistance arising from the electrolyte, electrode, and contact interfaces; $R_{ct}$, the charge-transfer resistance at the electrode–electrolyte interface; $C$, associated with the electric double-layer capacitance; and $Y_0$, representing Warburg diffusion. The fitted parameters obtained from EIS analysis are summarized in Table 2.

Table 2 Parameters obtained from Nyquist plot fitting

| Electroctalyst | $R_s$ (ohm) | $C_1$ (F) | $R_{ct}$ (ohm) | $Y_0$ |
|---|---|---|---|---|
| GP | 4.27 | $1.8 \times 10^{-11}$ | 102.9 | 0.122 |
| NiO-GP | 4.10 | $3.3 \times 10^{-6}$ | 2.4 | 0.806 |
| CoO-GP | 3.00 | $4.8 \times 10^{-6}$ | 5.8 | 0.870 |
| P-GP | 2.10 | $5.2 \times 10^{-6}$ | 4.7 | 0.872 |

Doping with oxygen-rich phosphorus groups results in a dramatic decrease in $R_{ct}$ from 102.9 Ω for GP to 4.7 Ω for P-GP, accompanied by a slight reduction in ohmic resistance. This substantial improvement arises from the abundance of oxygen functional groups, which act as active sites that facilitate charge transfer. Notably, P-GP also exhibits increases in both $C_1$ and $Y_0$, indicating enhanced electric double-layer capacitance and improved diffusion of vanadium ions at the electrode–electrolyte interface. A similar trend is observed for the CoO- and NiO-modified electrodes, where $R_{ct}$ decreases from 102.9 Ω to 5.8 Ω and 2.4 Ω, respectively, due to the presence of surface $O^{2-}$ species that provide additional catalytically active sites. These reductions in charge-transfer resistance further confirm the strong electrocatalytic activity of the introduced functional groups and metal oxides.

### 3.3. Full cell battery tests

The electrochemical performance of the VRFB using the GP electrode and the samples modified with CoO, NiO, or oxygen-rich phosphorus functional groups was evaluated through charge–discharge tests and polarization curve analysis. All measurements were carried out under identical conditions using an electrode area of 20 cm$^2$ and a constant current density of 50 mA cm$^{-2}$ within a potential window of 1.65–0.8 V. The coulombic efficiency (CE), voltage efficiency (VE), and energy efficiency (EE) were calculated using eqn (3)–(5), and the corresponding results are summarized in Table 4. Kinetic loss, area-specific resistance (ASR), and limiting current density were obtained from the polarization curves, as presented in Table 3.

The charge–discharge results show that the battery assembled with the oxygen-rich phosphorus–modified graphite electrode (P-GP) exhibits the longest operating time, the lowest charge-voltage plateau, and the highest discharge-voltage plateau, resulting in superior voltage and energy efficiencies (Fig. 5a).

Table 3 Comparison of overpotential, ASR, limiting current, and power density for the bare and modified electrodes

| Electrocatalyst | $\eta_{kinetics}$ (mV) | ASR ($\Omega$ cm$^2$) | $i_{lim}$ (mA cm$^{-2}$) | Power density (mW cm$^{-2}$) |
|---|---|---|---|---|
| GP | 0.93 | 9.45 | 64 | 49 |
| NiO-GP | 0.33 | 3.08 | 145 | 149 |
| CoO-GP | 0.32 | 2.85 | 144 | 154 |
| P-GP | 0.27 | 2.8 | 155 | 167 |

This electrode demonstrates the best overall performance, achieving CE, VE, and EE values of 96.55%, 87.27%, and 84.26%, respectively, at a current density of 50 mA cm$^{-2}$. These findings are consistent with the results of Kim *et al.*,[16] who reported that the introduction of phosphate groups enhances electrode wettability and suppresses the hydrogen evolution reaction, thereby improving redox reversibility. In comparison, both CoO- and NiO-modified electrodes show notable improvements over bare graphite. The CoO-GP electrode achieves CE, VE, and EE values of 92.5%, 93.07%, and 86.09%, while NiO-GP exhibits values of 90.8%, 88.48%, and 80.33%, confirming the beneficial effect of metal oxide functionalization on charge–discharge performance. The bare graphite (GP) electrode shows the lowest efficiencies, with CE, VE, and EE values of 89.11%, 88.01%, and 78.1%, demonstrating the clear advantage of surface modification in enhancing VRFB performance.

The superior performance of the P-GP electrode arises from its oxygen-rich phosphorus functional groups, which enhance surface wettability, improve ion transport, and suppress side reactions such as hydrogen evolution. Mechanistically, the phosphate groups introduce –OH functionalities capable of forming P–O–V interactions with vanadium species, creating localized electron-transfer centers that promote proton-coupled electron transfer during the $VO_2^+/VO^{2+}$ redox reaction. These interactions stabilize reaction intermediates, lower the charge-transfer resistance, and accelerate redox kinetics. Consequently, P-GP exhibits the lowest kinetic loss (0.27 mV), the lowest ASR (2.8 $\Omega$ cm$^2$), the highest limiting current (155 mA cm$^{-2}$), and the highest power density (167 mW cm$^{-2}$) among the evaluated electrodes. Among the metal-oxide-modified materials, CoO-GP outperforms NiO-GP, consistent with previous findings by Xiang *et al.*[43] CoO-GP displays slightly lower kinetic loss (0.32 *vs.* 0.33 mV), lower ASR (2.85 *vs.* 3.08 $\Omega$ cm$^2$), and higher power density (154 *vs.* 149 mW cm$^{-2}$), reflecting its higher intrinsic conductivity and stronger catalytic affinity for $VO_2^+$ species. The improved activity of CoO is attributed to its efficient electron-transfer characteristics and favorable interactions with vanadium ions. NiO-GP also enhances redox kinetics by introducing surface $O^{2-}$ species and carboxyl functionalities that improve vanadium-ion adsorption and electron transfer, though to a lesser extent than CoO. Both oxides improve wettability and reduce charge-transfer resistance; however, the superior catalytic behavior of CoO results in more favorable electrochemical performance[38] (Fig. 5b and c and Table 3).

To evaluate the rate capability and cycling behavior of the modified electrodes, charge–discharge tests were performed at various current densities (25, 50, 100, and 200 mA cm$^{-2}$), followed by a return to 25 mA cm$^{-2}$. As shown in Fig. 6b, the P-GP electrode delivers higher discharge capacities than the other samples across all current densities, including at 100 and 200 mA cm$^{-2}$, indicating improved redox kinetics and reduced polarization. When the current is returned to 25 mA cm$^{-2}$, the P-GP electrode recovers approximately 75% of its initial capacity, suggesting good electrochemical reversibility under the tested conditions (Table 5).

Table 4 Efficiencies of the VRFB cell using the GP NiO-GP, CoO-GP, and P-GP electrodes at the current density of 25 mA cm$^{-2}$

| Electrocatalyst | CE (%) | EE (%) | VE (%) |
|---|---|---|---|
| GP | 89.11 | 78.43 | 88.01 |
| NiO-GP | 90.79 | 80.33 | 88.48 |
| CoO-GP | 92.50 | 86.09 | 93.07 |
| P-GP | 94.41 | 88.72 | 93.97 |

Table 5 Efficiencies of the VRFB cell using P-GP electrode at current densities of 25, 50, 100, and 200 mA cm$^{-2}$

| Current density (mA cm$^{-2}$) | CE (%) | EE (%) | VE (%) |
|---|---|---|---|
| 25 | 94.41 | 88.72 | 93.97 |
| 50 | 96.55 | 84.26 | 87.27 |
| 100 | 97.34 | 74.94 | 76.99 |
| 200 | 98.42 | 64.32 | 65.35 |

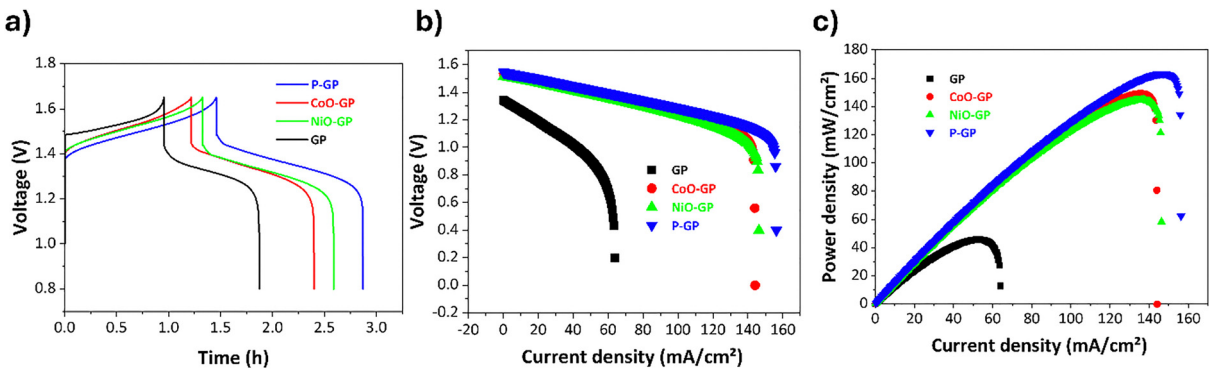


Fig. 5 Electrochemical cycling performance of bare GF and modified electrodes. (a) Charge/discharge voltage profiles at a 50 mA cm$^{-2}$ current density. (b) Polarization curves of VRFB cells assembled with bare and modified electrodes. And (c) the power density peaks of the VRRB cell.

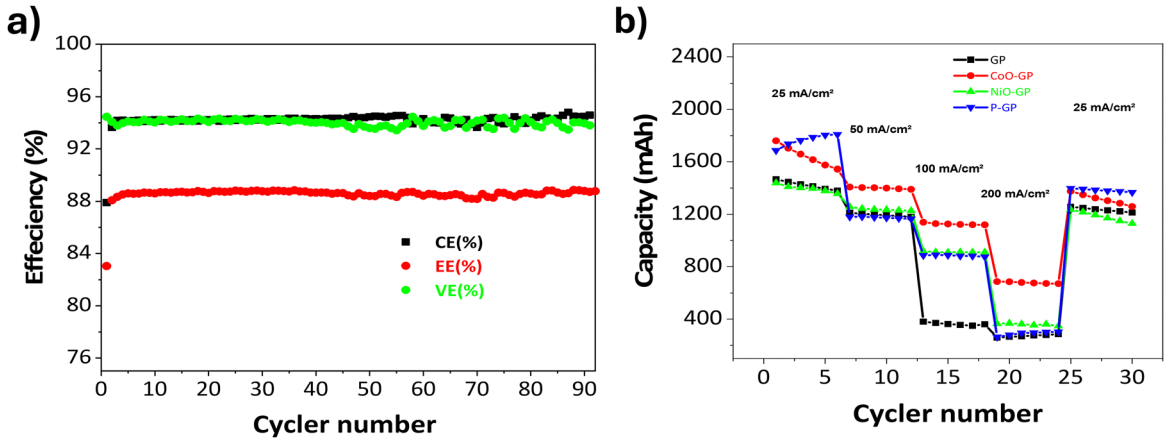


Fig. 6 (a) EE, CE, and VE over 90 charging–discharging cycles of the cell containing P-GP at a current density of 25 mA $cm^{-2}$, (b) rate performance of GP-based electrodes at various current densities.

The CoO-GP electrode also maintains its capacity as the current density increases, with a recovery of about 79% when the current is reduced, consistent with its electrocatalytic activity toward the vanadium redox reactions. The NiO-GP electrode shows moderate capacity retention and lower discharge capacity relative to CoO-GP and P-GP, reflecting slower redox kinetics; however, it achieves a capacity recovery of about 83% upon returning to a lower current. The unmodified graphite (GP) electrode exhibits a pronounced decrease in capacity at higher current densities and limited recovery thereafter, consistent with higher internal resistance and reduced electrochemical activity.

Fig. 6a presents the cycling performance of the VRFB employing the P-GP electrode over 90 charge–discharge cycles at 25 mA $cm^{-2}$. The Coulombic efficiency (CE) remains stable at approximately 96%, indicating low self-discharge and effective utilization of vanadium ions. The voltage efficiency (VE) remains around 92%, reflecting low polarization and stable internal resistance during the test. As a result, the energy efficiency (EE) stays consistently near ~84%. The minimal variation in the efficiency metrics indicates that the P-GP electrode maintains steady electrochemical activity throughout the evaluated cycling period, consistent with the behavior reported for other surface-modified graphite electrodes used to enhance the $VO_2^+/VO^{2+}$ redox reaction.

As shown in Table 6, the P-GP sample exhibits a voltage efficiency of 76.9% at a current density of 100 mA $cm^{-2}$, which is comparable to values reported for phosphorus-functionalized graphite felt under similar operating conditions. The corresponding energy efficiency of 74.9% is also higher than that reported for several other phosphorus- or heteroatom-functionalized graphite felt electrodes. It is important to note that the preparation approach used in this work is simpler and more cost-effective, as it employs graphite powder rather than graphite felt as the support material. For the metal oxide–modified graphite powder electrodes, NiO@-graphite and CoO@graphite show voltage efficiencies of 88.4% and 86.0%, respectively, and energy efficiencies of 80.3% and 93.0% at 25 mA $cm^{-2}$. These values are consistent with those reported for NiO- and CoO-modified graphite felt in earlier studies. The corresponding power densities of 149 mW $cm^{-2}$ (NiO-graphite) and 154 mW $cm^{-2}$ (CoO-graphite) further indicate that graphite powder, despite its lower cost, can support electrocatalytic performance comparable to felt-based systems.

## 4. Conclusion

In this study, the electrocatalytic performance of graphite powder electrodes modified with CoO, NiO, and oxygen-rich phosphorus

Table 6 Comparison of notable modification approaches of graphite felt, carbon fiber, and graphite powder electrodes for VRFB study

| Materials | Support material | CE% | VE% | EE% | Power density (mW $cm^{-2}$) | Current density (mA $cm^{-2}$) | Ref. |
|---|---|---|---|---|---|---|---|
| Reduced graphene oxide/MXene@GF | Graphite felt | 91.6 | 82.7 | 75.8 | — | 80 | 44 |
| Metal–organic-framework-derived ZnO–$Fe_2O_3$@GF | Graphite felt | 96.5 | 87 | 84 | — | 150 | 45 |
| Binder-free CNT-modified graphite felt (CNT-GFs) | Graphite felt | 97 | 85 | 82 | — | 100 | 46 |
| CVD-grown CNTs-modified graphite felt | Graphite felt | 96.3 | 79.3 | 76.3 | — | — | 47 |
| Taurine-functionalized carbon nanotubes | Graphite felt | 96.8 | 81.4 | 78.8 | — | 300 | 18 |
| Nitrogen-phosphorus co-doped carbon fiber | Carbon fiber | ~94 | ~80 | ~72 | — | — | 15 |
| Carbon felt @oxygen-rich phosphate | Carbon felt | ~95 | ~93 | 88.2 | — | 32 | 16 |
| NiO distributed on graphite felt | Graphite felt | ~97 | ~76 | 74.5 | — | 125 | 38 |
| Graphene nanosheet | Graphite | 98 | 69 | 70 | — | 150 | 32 |
| CoO distributed on graphite felt | Graphite felt | 89.5 | 77.6 | 69.4 | 260 | 150 | 43 |
| Oxygen–phosphorus-graphite | Graphite powder | 97.3 | 76.9 | 74.9 | 167 | 100 | Our work |
| NiO-graphite | Graphite powder | 90.7 | 88.4 | 80.3 | 149 | 25 | Our work |
| CoO-graphite | Graphite powder | 92.5 | 86 | 93 | 154 | 25 | Our work |

functional groups (P-GP) was systematically investigated to address the kinetic limitations of the $VO_2^+/VO^{2+}$ redox couple in vanadium redox flow batteries (VRFBs). Incorporation of these functional materials enhanced electrochemical activity, as demonstrated by changes in cyclic voltammetry profiles, reduced charge-transfer resistance from EIS measurements, and increased efficiencies during charge–discharge cycling. Among the modified electrodes, the P-GP material showed higher coulombic efficiency (94.41%), voltage efficiency (93.97%), energy efficiency (88.72%) at 25 mA $cm^{-2}$, and greater power density (167 mW $cm^{-2}$) relative to unmodified graphite. The CoO- and NiO-modified electrodes also delivered improvements in electrochemical metrics and power output. The P-GP electrode maintained stable coulombic efficiency over 90 cycles, indicating short-term operational stability under the tested conditions. Overall, these results demonstrate that surface functionalization, particularly phosphorus-based modification, offers a cost-effective and scalable approach for enhancing graphite powder electrodes in VRFB systems beyond graphite felt and may contribute to the development of cost-effective energy storage technologies.

## Conflicts of interest

There are no conflicts to declare.

## Data availability

The data generated in this research are available upon request.

The supplementary information contains additional supporting figures. See DOI: https://doi.org/10.1039/d5ya00381d.

## Acknowledgements

The authors express their gratitude to the Office Chérifien des Phosphates (OCP S. A.) and Mohammed VI Polytechnic University for their invaluable financial support.

## References

1 D. J. Davidson, Exnovating for a Renewable Energy Transition, *Nat. Energy*, 2019, **4**, 254–256, DOI: 10.1038/s41560-019-0369-3.

2 A. T. D. Perera, V. M. Nik, D. Chen, J.-L. Scartezzini and T. Hong, Quantifying the Impacts of Future Climate Variations and Extreme Climate Events on Energy Systems, *Nat. Energy*, 2020, **5**(2), 150–159, DOI: 10.1038/s41560-020-0558-0.

3 V. Masson-Delmotte, H.-O. Pörtner, J. Skea, P. Zhai, D. Roberts, P. R. Shukla, A. Pirani, R. Pidcock, Y. Chen, E. Lonnoy, W. Moufouma-Okia, C. Péan, S. Connors, J. B. R. Matthews, X. Zhou, M. I. Gomis, T. Maycock, M. Tignor and T. Waterfield, *An IPCC Special Report on the Impacts of Global Warming of 1.5 °C above Pre-Industrial Levels and Related Global Greenhouse Gas Emission Pathways, in the Context of Strengthening the Global Response to the Threat of Climate Change*, Sustainable Development, and Efforts to Eradicate Poverty; IPCC, Geneva, 2018.

4 P. Achakulwisut, Global Fossil Fuel Reduction Pathways under Different Climate Mitigation Strategies and Ambitions, *Nat. Commun.*, 2023, **14**, 5425, DOI: 10.1038/s41467-023-41105-z.

5 Z. Yang, J. Zhang, M. C. W. Kintner-Meyer, X. Lu, D. Choi, J. P. Lemmon and J. Liu, Electrochemical Energy Storage for Green Grid, *Chem. Rev.*, 2011, **111**, 3577–3613, DOI: 10.1021/cr100290v.

6 A. Kalair, N. Abas, M. S. Saleem, A. R. Kalair and N. Khan, Role of Energy Storage Systems in Energy Transition from Fossil Fuels to Renewables, *Energy Storage*, 2020, **3**(1), DOI: 10.1002/est2.135.

7 G. L. Soloveichik, Flow Batteries: Current Status and Trends, *Chem. Rev.*, 2015, **115**(20), 11533–11558, DOI: 10.1021/cr500720t.

8 M. Skyllas-Kazacos, Redox Flow Batteries for Medium-to Large-Scale Energy Storage, *Electricity Transmission, Distribution and Storage Systems*, 2013, vol. 3, pp. 398–441, DOI: 10.1533/9780857097378.3.398.

9 B. Dunn, H. Kamath and J.-M. Tarascon, Electrical Energy Storage for the Grid: A Battery of Choices, *Science*, 2011, **334**, 928–935, DOI: 10.1126/science.1212741.

10 Y. Wang, Research on All-Vanadium Redox Flow Battery Energy Storage Device Based on Energy-Saving and Environmentally-Friendly New Energy Power Station Interface Technology, *OP Conf. Ser.: Earth Environ. Sci.*, 2021, **651**, 022097, DOI: 10.1088/1755-1315/651/2/022097.

11 W. Wang, Q. Luo, B. Li, X. Wei, L. Li and Z. Yang, Recent Progress in Redox Flow Battery Research and Development, *Adv. Funct. Mater.*, 2013, **23**, 970–986, DOI: 10.1002/adfm.201200694.

12 P. Alotto, Redox Flow Batteries for the Storage of Renewable Energy_ A Review, *Renewable Sustainable Energy Rev.*, 2014, **29**, 325–335, DOI: 10.1016/j.rser.2013.08.001.

13 B. Shanahan, K. Seteiz, P. A. Heizmann, S. Koch, J. Büttner, S. Ouardi, S. Vierrath, A. Fischer and M. Breitwieser, Rapid Wet-Chemical Oxidative Activation of Graphite Felt Electrodes for Vanadium Redox Flow Batteries, *RSC Adv.*, 2021, **11**(51), 32095–32105, DOI: 10.1039/D1RA05808H.

14 Q. Jiang, Y. Ren, Y. Yang, L. Wang, L. Dai and Z. He, Recent Advances in Carbon-Based Electrocatalysts for Vanadium Redox Flow Battery: Mechanisms, Properties, and Perspectives, *Composites, Part B*, 2022, **242**, 110094, DOI: 10.1016/j.compositesb.2022.110094.

15 X. Chen, C. Wu, Y. Lv, S. Zhang, Y. Jiang, Z. Feng, L. Wang, Y. Wang, J. Zhu, L. Dai and Z. He, Highly Active Nitrogen-Phosphorus Co-Doped Carbon Fiber@graphite Felt Electrode for High-Performance Vanadium Redox Flow Battery, *J. Colloid Interface Sci.*, 2025, **677**, 683–691, DOI: 10.1016/j.jcis.2024.08.091.

16 K. J. Kim, H. S. Lee, J. Kim, M.-S. Park, J. H. Kim, Y.-J. Kim and M. Skyllas-Kazacos, Superior Electrocatalytic Activity of a Robust Carbon-Felt Electrode with Oxygen-Rich Phosphate Groups for All-Vanadium Redox Flow Batteries, *ChemSusChem*, 2016, **9**(11), 1329–1338, DOI: 10.1002/cssc.201600106.

17 K. Amini, J. Gostick and M. D. Pritzker, Metal and Metal Oxide Electrocatalysts for Redox Flow Batteries, *Adv. Funct. Mater.*, 2020, **30**(23), 1910564, DOI: 10.1002/adfm.201910564.

18 L. Wei, T. Liu, Y. Zhang, H. Liu and L. Ge, Taurine-Functionalized Carbon Nanotubes as Electrode Catalysts for Improvement in the Performance of Vanadium Redox Flow Battery, *Catalysts*, 2024, **14**(4), 281, DOI: 10.3390/catal14040281.
19 G. Dey, S. Saifi, H. Sharma, M. Kumar and A. Aijaz, Carbon Nanofibers Coated with MOF-Derived Carbon Nanostructures for Vanadium Redox Flow Batteries with Enhanced Electrochemical Activity and Power Density, *ACS Appl. Nano Mater.*, 2023, **6**(10), 8684–8697, DOI: 10.1021/acsanm.3c01334.
20 J. Su, Z. Li, L. Hao and L. Qin, Preparation and Electrocatalytic Activity of a Cobalt Mixed Nitrogen 3D Carbon Nanostructure @ Carbon Felt toward an All-Vanadium Redox Flow Battery, *Appl. Sci.*, 2022, **12**(5), 2304, DOI: 10.3390/app12052304.
21 C. Zhao, Y. Li, Z. He, Y. Jiang, L. Li, F. Jiang, H. Zhou, J. Zhu, W. Meng, L. Wang and L. Dai, $KHCO_3$ Activated Carbon Microsphere as Excellent Electrocatalyst for $VO^{2+}/VO^{2+}$ Redox Couple for Vanadium Redox Flow Battery, *J. Energy Chem.*, 2019, **29**, 103–110, DOI: 10.1016/j.jechem.2018.02.006.
22 Z. He, L. Dai, S. Liu, L. Wang and C. Li, $Mn_3O_4$ Anchored on Carbon Nanotubes as an Electrode Reaction Catalyst of V(IV)/V(V) Couple for Vanadium Redox Flow Batteries, *Electrochim. Acta*, 2015, **176**, 1434–1440, DOI: 10.1016/j.electacta.2015.07.067.
23 X. Wu, H. Xu, L. Lu, H. Zhao, J. Fu, Y. Shen, P. Xu and Y. Dong, $PbO_2$-Modified Graphite Felt as the Positive Electrode for an All-Vanadium Redox Flow Battery, *J. Power Sources*, 2014, **250**, 274–278, DOI: 10.1016/j.jpowsour.2013.11.021.
24 S. Mousavihashemi, S. Murcia-López, M. A. Rodriguez-Olguin, H. Gardeniers, T. Andreu, J. R. Morante, A. Susarrey Arce and C. Flox, Overcoming Voltage Losses in Vanadium Redox Flow Batteries Using $WO_3$ as a Positive Electrode, *ChemCatChem*, 2022, **14**(23), e202201106, DOI: 10.1002/cctc.202201106.
25 J. Vázquez-Galván, C. Flox, J. R. Jervis, A. B. Jorge, P. R. Shearing and J. R. Morante, High-Power Nitrided $TiO_2$ Carbon Felt as the Negative Electrode for All-Vanadium Redox Flow Batteries, *Carbon*, 2019, **148**, 91–104, DOI: 10.1016/j.carbon.2019.01.067.
26 W.-J. Lee, T.-W. Hsu, W.-L. Lee, T. T. Thai and C.-C. Chen, Surface Modification of Carbon Felt Electrodes with $SnO_2$ Nanocoatings by Using the SILAR Method for Enhanced Performance in Vanadium Redox Flow Batteries, *Appl. Surf. Sci.*, 2025, **686**, 162150, DOI: 10.1016/j.apsusc.2024.162150.
27 Y. Xiang and W. A. Daoud, Binary $NiCoO_2$-Modified Graphite Felt as an Advanced Positive Electrode for Vanadium Redox Flow Batteries, *J. Mater. Chem. A*, 2019, **7**(10), 5589–5600, DOI: 10.1039/C8TA09650C.
28 M. Cermak, N. Perez, M. Collins and M. Bahrami, Material Properties and Structure of Natural Graphite Sheet, *Sci. Rep.*, 2020, **10**(1), 18672, DOI: 10.1038/s41598-020-75393-y.
29 J. Asenbauer, T. Eisenmann, M. Kuenzel, A. Kazzazi, Z. Chen and D. Bresser, The Success Story of Graphite as a Lithium-Ion Anode Material – Fundamentals, Remaining Challenges, and Recent Developments Including Silicon (Oxide) Composites, *Sustainable Energy Fuels*, 2020, **4**(11), 5387–5416, DOI: 10.1039/D0SE00175A.
30 Y.-D. Kuan, C.-W. Ciou, M.-Y. Shen, C.-K. Wang, R. Z. Fitriani and C.-Y. Lee, Bipolar Plate Design and Fabrication Using Graphite Reinforced Composite Laminate for Proton Exchange Membrane Fuel Cells, *Int. J. Hydrogen Energy*, 2021, **46**(31), 16801–16814, DOI: 10.1016/j.ijhydene.2020.08.030.
31 Z. Chen, J. Wen, C. Yan, L. Rice, H. Sohn, M. Shen, M. Cai, B. Dunn and Y. Lu, High-Performance Supercapacitors Based on Hierarchically Porous Graphite Particles, *Adv. Energy Mater.*, 2011, **1**(4), 551–556, DOI: 10.1002/aenm.201100114.
32 M. Park, I. Jeon, J. Ryu, J. Baek and J. Cho, Exploration of the Effective Location of Surface Oxygen Defects in Graphene-Based Electrocatalysts for All-Vanadium Redox-Flow Batteries, *Adv. Energy Mater.*, 2015, **5**(5), 1401550, DOI: 10.1002/aenm.201401550.
33 A. Alazmi, C. T.-C. Wan, P. M. F. J. Costa and F. R. Brushett, Exploration of Reduced Graphene Oxide Microparticles as Electrocatalytic Materials in Vanadium Redox Flow Batteries, *J. Energy Storage*, 2022, **50**, 104192, DOI: 10.1016/j.est.2022.104192.
34 Y. Seffar, A. S. Idrissi, J. Alami and M. Dahbi, Exploring Anthracite-Derived Microporous Activated Carbon for Efficient and Sustainable Electrochemical Desalination in Capacitive Deionization Cell, *ChemistrySelect*, 2025, **10**(23), e04368, DOI: 10.1002/slct.202404368.
35 N. El Halya, M. Aqil, K. El Ouardi, A. Bano, A. El Bendali, L. Hdidou, R. Amine, S. Son, F. Ghamouss, D. T. Major, K. Amine, J. Alami and M. Dahbi, Biopolymer-assisted Synthesis of P-doped $TiO_2$ Nanoparticles for High-performance Lithium-ion Batteries: A Comprehensive Study, *Batteries Supercaps*, 2024, **7**(1), e202300424, DOI: 10.1002/batt.202300424.
36 A. S. Idrissi, Y. Seffar, A. E. Bendali, J. Alami, H. Sehaqui and M. Dahbi, Recovery of Spent Activated Carbon from Treatment Plants for High Performance Electrodes in Capacitive Deionization Processes, *Electrochim. Acta*, 2025, **513**, 145446, DOI: 10.1016/j.electacta.2024.145446.
37 S. Kalasina, K. Kongsawatvoragul, N. Phattharasupakun, P. Phattharaphuti and M. Sawangphruk, Cobalt Oxysulphide/Hydroxide Nanosheets with Dual Properties Based on Electrochromism and a Charge Storage Mechanism, *RSC Adv.*, 2020, **10**(24), 14154–14160, DOI: 10.1039/D0RA01714K.
38 N. Yun, J. J. Park, O. O. Park, K. B. Lee and J. H. Yang, Electrocatalytic Effect of NiO Nanoparticles Evenly Distributed on a Graphite Felt Electrode for Vanadium Redox Flow Batteries, *Electrochim. Acta*, 2018, **278**, 226–235, DOI: 10.1016/j.electacta.2018.05.039.
39 X. He, X. Song, W. Qiao, Z. Li, X. Zhang, S. Yan, W. Zhong and Y. Du, Phase- and Size-Dependent Optical and Magnetic Properties of CoO Nanoparticles, *J. Phys. Chem. C*, 2015, **119**(17), 9550–9559, DOI: 10.1021/jp5127909.
40 Z. Wei, H. Qiao, H. Yang, C. Zhang and X. Yan, Characterization of NiO Nanoparticles by Anodic Arc Plasma Method, *J. Alloys Compd.*, 2009, **479**(1–2), 855–858, DOI: 10.1016/j.jallcom.2009.01.064.
41 N. El Halya, M. Kerroumi, E. H. Elmaataouy, A. Amarray, M. Aqil, J. Alami and M. Dahbi, Limiting Voltage and Capacity Fade of Lithium-Rich, Low Cobalt $Li_{1.2}Ni_{0.13}Mn_{0.54}Fe_{0.1}Co_{0.03}O_2$ by Controlling the Upper Cut-off Voltage, *RSC Adv.*, 2023, **13**(49), 34416–34426, DOI: 10.1039/D3RA06873K.
42 R. Wang, Y. Li, Y. Wang and Z. Fang, Phosphorus-Doped Graphite Felt Allowing Stabilized Electrochemical Interface

and Hierarchical Pore Structure for Redox Flow Battery, *Appl. Energy*, 2020, **261**, 114369, DOI: 10.1016/j.apenergy.2019.114369.

43 Y. Xiang and W. A. Daoud, Investigation of an Advanced Catalytic Effect of Cobalt Oxide Modification on Graphite Felt as the Positive Electrode of the Vanadium Redox Flow Battery, *J. Power Sources*, 2019, **416**, 175–183, DOI: 10.1016/j.jpowsour.2019.01.079.

44 Z. Li, W. Yang, J. Bao, Y. Kong, S. Jing, J. Zhang, G. Ren, L. Sun and M. Du, Reduced Graphene Oxide/MXene Hybrid Decorated Graphite Felt as an Effective Electrode for Vanadium Redox Flow Battery, *RSC Adv.*, 2024, **14**(17), 12158–12170, DOI: 10.1039/D4RA01306A.

45 P. Lakshmanan, C.-H. Huang, S. D. Rengapillai, Y.-S. Chen, W.-R. Liu, C.-L. Hsu and S. Marimuthu, Graphite Felt Decorated with Metal–Organic Framework-Derived Nanocomposite as Cathode for Vanadium Redox Flow Battery, *Nanomaterials*, 2025, **15**(7), 535, DOI: 10.3390/nano15070535.

46 N. Devi, P. Singh and Y.-S. Chen, Binder-Free CNT-Modified Excellent Electrodes for All-Vanadium Redox Flow Batteries, *Nanomaterials*, 2024, **14**(9), 767, DOI: 10.3390/nano14090767.

47 Y.-S. Chou, N. Devi, Y.-T. Lin, A. Arpornwichanop and Y.-S. Chen, CVD Grown CNTs-Modified Electrodes for Vanadium Redox Flow Batteries, *Materials*, 2024, **17**(13), 3232, DOI: 10.3390/ma17133232.